

Research Paper

Stirling pulse tube cryocooler using an active displacer

Mohammad Amin Abolghasemi^{a,*}, Kun Liang^b, Richard Stone^a, Mike Dadd^a, Paul Bailey^a

^a Department of Engineering Science, University of Oxford, UK

^b Department of Engineering and Design, University of Sussex, UK



ARTICLE INFO

Keywords:

Stirling cycle

Pulse tube

Cryocooler

Active displacer

Phase optimisation

ABSTRACT

An in-line pulse tube cryocooler with an active displacer has been built and its performance has been examined in detail by experimental measurements and numerical modelling. An active displacer allows the mass flow at the cold end to be easily adjusted for optimum performance. It is demonstrated that both cooling power and relative Carnot efficiency have optimum phase values that are different. It is also shown that the phase optimisations are not critical – good performance is achieved over a significant range. The pulse tube cryocooler can deliver up to 3.8 W of cooling at 80 K with an input power of 88 W (shaft power of 69 W) when operating at optimal phase. Moreover, a numerical Sage model is used to enhance our understanding behind the trends observed by examining the mass flow and pressure pulse at the cold end. It is shown that the variation in phase of the active displacer helps boost the cryocooler performance by increasing the amplitude of the mass flow at the cold end and not by adjusting the phase of the mass flow. The Sage model is also used to demonstrate that using a displacer in place of an inertance tube can result in a more efficient cryocooler.

1. Introduction

Stirling pulse tube cryocoolers (SPTCs) are small low temperature refrigerators that can provide cooling for electronic devices such as infra-red detectors and superconducting devices. The operation of SPTCs involve complex thermodynamics which are not always intuitively understood. One of the main requirements for successful operation is the need for the correct relationship between the mass flow and the pressure pulse at the cold end. It has been suggested that a 30° lag between the mass flow and the pressure pulse is the approximate optimum [1]. This is usually achieved via the use of an orifice [2–4], an inertance tube [5–7] or a warm end displacer [8–10]. Orifices and inertance tubes are commonly used as they avoid the need for any moving components in the cold head assembly and therefore reduce potential vibrations. However, with these mechanisms the mass flow is not readily controlled. It is therefore difficult to ensure that the SPTC is operating with an optimum relationship between the mass flow and the pressure pulse at the cold end.

On the other hand, a displacer allows the phase to be tuned and is therefore beneficial when trying to investigate the performance of an SPTC. When using a displacer, the mass flow at the cold end can be adjusted by varying the phase between the displacer motion and the linear compressor piston motion. The displacer at the warm end can be either driven (i.e. active) or free-moving, where the motion of the

displacer depends on its fill pressure, damping and natural frequency [9]. Furthermore, Zhu et al. [9] suggested that the expansion power at the warm end of the pulse tube, which is otherwise dissipated as heat when using an orifice or an inertance tube, can be recovered via the displacer and the SPTC can operate more efficiently. Recently, Shi et al. [10] investigated the performance of a coaxial SPTC with a free moving displacer. Therein, it was demonstrated that recovering the expansion power via a displacer can help improve the efficiency of an SPTC. However, sensitivity to phase was not analysed as this required changing the natural frequency of the displacer by varying its mass, spring stiffness and/or rod diameter [10].

For the present study, an in-line SPTC with an active displacer has been designed and built. Hence, the phase can be easily adjusted during operation and the performance of the SPTC can be optimised. Initially, the SPTC design is introduced, along with the instrumentation and the experimental setup. Section 3 sets out the numerical model developed in Sage [11]. The SPTC performance was experimentally tested for a range of different fill pressures and frequencies and this data is used to validate the numerical Sage model. Phase optimisation is discussed in Section 4 and the performance of the active displacer SPTC is compared against an SPTC with an inertance tube using the Sage model in Section 5.

* Corresponding author.

E-mail address: amin.abolghasemi@eng.ox.ac.uk (M.A. Abolghasemi).

Nomenclature

| | |
|------------------|---|
| \dot{m} | mass flow (g/s) |
| $\dot{W}_{in,c}$ | linear compressor input power (W) |
| $\dot{W}_{in,d}$ | displacer input power (W) |
| \dot{W}_{in} | total input power (W) |
| $\dot{W}_{sh,c}$ | linear compressor shaft power (W) |
| $\dot{W}_{sh,d}$ | displacer shaft power (W) |
| \dot{W}_{sh} | total shaft power (W) |
| η_m | linear compressor motor efficiency |
| η_r | relative Carnot efficiency based on shaft power |
| ϕ_d | phase angle between position of linear compressor and displacer |

| | |
|-------------|---|
| ϕ_{pm} | phase angle between pressure pulse and mass flow |
| d_c | linear compressor stroke (mm) |
| d_d | displacer stroke (mm) |
| f | operating frequency (Hz) |
| I_c | linear compressor current (A) |
| P_1 | pressure pulse at the warm end of the regenerator (bar) |
| P_2 | pressure pulse at the warm end of the pulse tube (bar) |
| Q_c | cooling power (W) |
| R_c | linear compressor coil resistance (Ω) |
| T_c | cold end temperature (K) |
| T_h | heat rejection temperature (K) |

2. Design and instrumentation

2.1. Design

The experimental setup and the instrumentation used for this study are illustrated in Fig. 1. The apparatus consists of

- An oil-free dual piston moving coil linear compressor capable of operating at frequencies up to 70 Hz. The linear compressor supplies a pressure wave that drives the closed thermodynamic cycle.
- An aftercooler (HX1 in Fig. 1) which is a finned annulus copper heat exchanger.
- A regenerator densely packed with stainless steel 400-mesh (wires per inch).
- A cold end heat exchanger (HX2 in Fig. 1) which is packed with copper 50-mesh (wires per inch). This is where the lowest temperature is achieved.
- A pulse tube where the temperature gradually rises back up to ambient.

- A warm end heat exchanger (HX3 in Fig. 1) which is also packed with copper 50-mesh (wires per inch).
- A single piston oil free active displacer which was powered separately and used to adjust the relationship between the pressure pulse and the mass flow at the cold end.

The aftercooler (HX1 in Fig. 1) and the warm end of the pulse tube (HX3 in Fig. 1) were both kept at ambient temperature via water cooled housings. Moreover, the cold head assembly, consisting of the regenerator and the pulse tube, was housed inside a vacuum chamber in order to minimise convective losses. A vacuum with pressures below 1×10^{-5} mbar (measured at the inlet to the vacuum system) was maintained throughout the experiments. Radiation shields were also wrapped around the cold head assembly in order to minimise heat losses via radiation. The cold head assembly is shown in more detail in Fig. 2.

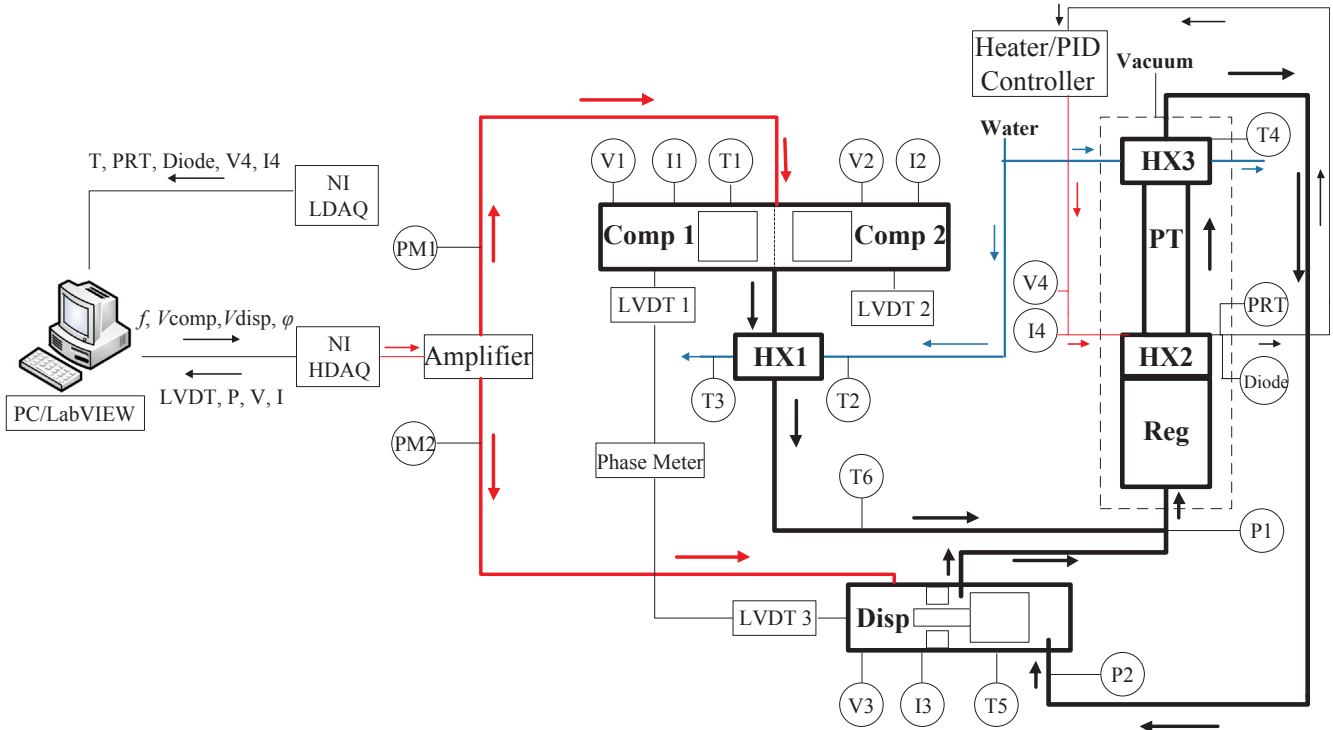


Fig. 1. The experimental layout with abbreviations **Comp** for compressor, **Disp** for active displacer, **Reg** for regenerator, **PT** for pulse tube, **HX** for heat exchanger, **HDAQ** for high speed data acquisition, **LDAQ** for low speed data acquisition, **LVDT** for linear variable differential transformers, **P** for pressure transducer, **T** for thermocouple and **PM** for power meter.

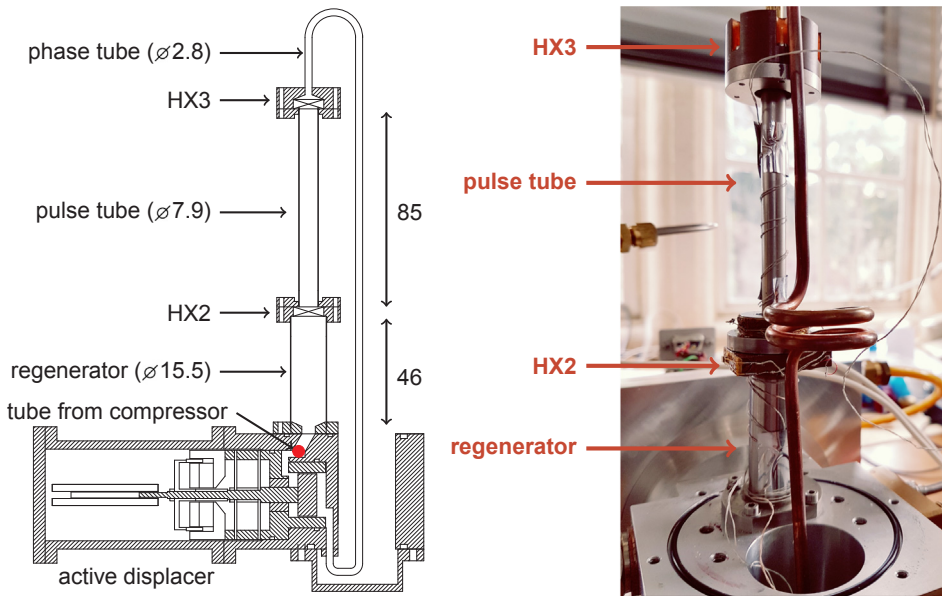
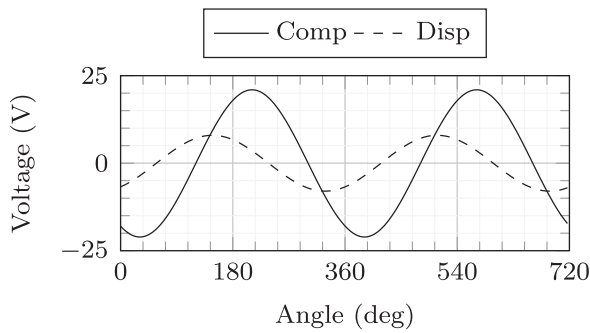


Fig. 2. The cold head assembly with the vacuum chamber removed and before it was wrapped in radiation shields. The same abbreviations as in Fig. 1. The drawing shows how the back space of the active displacer is connected to the warm end of the regenerator. The location where the connecting tube from the linear compressor joins the cold head assembly is also shown. All dimensions are in millimeters.

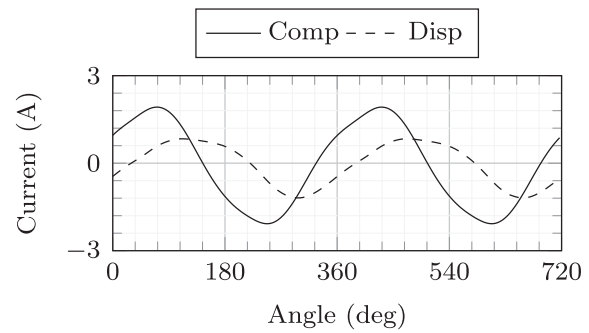
2.2. Instrumentation

The displacements of the compressor and the active displacer were controlled via a sinusoidal waveform defined by the user. The signals were generated in LabVIEW® and were amplified and then delivered to the components via power meters. The frequency of operation as well as the amplitude of both the compressor and the active displacer motion were set by the user. Furthermore, the driving voltage phase angle difference between the compressor and the active displacer was also user defined.

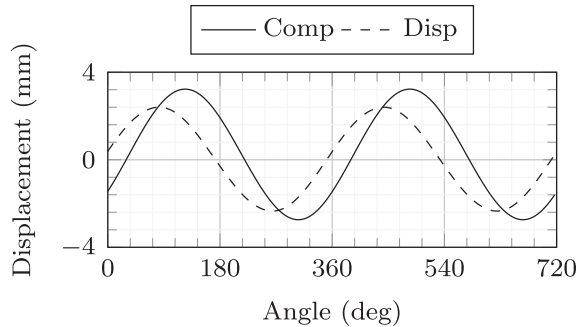
Linear variable differential transformer (LVDT) displacement transducers were used to record the position of the pistons for both the compressor and the active displacer. This information was transferred to the PC via the high speed data acquisition (HDAQ) card. As well as the amplitude of the oscillations, the phase angle between the compressor and the displacer was recorded via a phase meter. Moreover, two piezoresistive pressure transducers were used to record the instantaneous pressure either side of the active displacer for comparisons against the Sage numerical model. A sampling rate of 5 kHz was used for the HDAQ data.



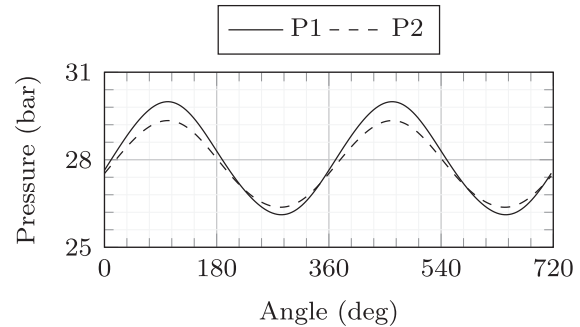
(a) Sample voltages



(b) Sample currents



(c) Sample displacements



(d) Sample pressure pulses

Fig. 3. Voltage, current, and displacements data recorded for the linear compressor and the active displacer. The pressure pulses either side of the active displacer is also shown. The operating frequency was 55 Hz with a fill pressure of 28 bar.

The cold end temperature was recorded using two sensors: A platinum resistor thermometer (PRT) and a silicon diode cryogenic temperature sensor. A Lakeshore temperature PID controller was used to maintain a user defined cold end temperature by adjusting the heater power. Due to better positioning in the cold end copper block, the PRT data was used as the reference cold end temperature in this study. The reason for this is discussed in more detail in Section 2.3. Temperatures at various other locations within the system were recorded using thermocouples as indicated in Fig. 1. All temperature values were recorded and logged in LabVIEW via the low speed data acquisition (LDAQ) card with a sampling rate of 10 Hz.

Fig. 3 shows an example of the HDAQ data obtained from one of the tests. It shows the linear compressor and displacer voltages (Fig. 3a), currents (Fig. 3b) and displacements (Fig. 3c). It also shows the pressure pulses recorded either side of the active displacer by the pressure transducers (Fig. 3d). Note how the current signal is not sinusoidal (Fig. 3b). This is due to the non-sinusoidal counter-electromotive force (i.e. back emf) generated by the varying magnetic induction inside the linear compressor coils. In the example shown the strokes are 6.0 mm in the linear compressor pistons and 4.8 mm in the active displacer and the displacer motion lags the linear compressor pistons by 42°. It is by adjusting this phase angle that the performance of the SPTC can be optimised. This is discussed further in Section 4.

2.3. Cold end temperature measurements

During the experiments, it was observed that the PRT readings did not agree with the silicon diode cryogenic temperature sensor readings for T_c . A correlation between the difference of the two readings and the amount of heater input power was observed in Fig. 4. Note that no sensitivity to fill pressure is observed. It is suspected that this correlation is due to the positioning of the two sensors. The silicon diode sensor (expected accuracy $\pm 0.25\%$) was externally glued onto the side of the cold head copper block, whereas the PRT (expected accuracy $\pm 1\%$) was positioned in a cylindrical hole drilled into the side of the cold head. Hence, the variation in reading is most probably due to temperature gradients within the cold head imposed by the heater. There is also a 2.5 K difference between the two sensors even when there is no heat load. The authors suspect that this is due to poor contact between the diode sensor and the cold head.

Given that the PRT was closer to the gas (better thermal contact) and registers a colder temperature, the T_c values quoted in this study are those obtained via the PRT. In future, the positioning of the temperature sensors will be carefully designed in order to prevent thermal interaction problems. In the context of the experimental results presented, this simply means that the cold end temperature might be (at worst) 2.5 K higher than the quoted value. This has no influence on the relative performance curves presented and does not affect the conclusions drawn from this study.

2.4. Static losses

Quantifying and minimising the static losses is important as it helps improve the efficiency of the cryocooler. In order to determine the static losses, the SPTC was switched off at $T_c = 65$ K and, at exactly the same time, a heat load was applied at the cold end. The time for the cold end temperature to rise from 75 K to 85 K was logged. The reciprocal of time is plotted against the heat load as shown in Fig. 5. There is a linear relationship between the reciprocal of time and heat put in. It is argued that this linear relationship extends to heat removed as well. By extrapolating the line in Fig. 5, the vertical axis intercept can be found. This is the amount of heat removed for which the cool down time is infinite. In other words, this is the cooling required to maintain 80 K. Hence, the static losses for the SPTC were 1.3 W at 80 K.

Static losses include radiation, convection and conduction losses. Radiation losses have been limited via the use of radiation shields.

Convective losses in the regenerator are expected to be small thanks to the densely packed wire mesh. In the pulse tube, convective losses should be small due the pulse tube orientation. The static losses value quoted here is primarily the axial thermal conduction loss. This can be further reduced by improving the vacuum and also improving the radiation shields that were wrapped around the cold head assembly.

2.5. Motor efficiency

For optimum motor efficiency, the linear compressor should be operated at or close to resonance. In order to determine the optimal operating frequency of the linear compressor at different fill pressures at $T_c = 80$ K, the motor efficiency, η_m , as a function of frequency was examined, Fig. 6a. The motor efficiency was calculated using

$$\dot{W}_{sh,c} = \dot{W}_{in,c} - I_c^2 R_c, \quad (1)$$

$$\eta_m = \frac{\dot{W}_{sh,c}}{\dot{W}_{in,c}}, \quad (2)$$

where $\dot{W}_{in,c}$ and $\dot{W}_{sh,c}$ are the linear compressor electrical input and shaft power, respectively. The linear compressor current is I_c and the coil resistance is R_c . Here the copper loss (i.e. $I^2 R$ loss) is considered to be the main loss. This is because when using force-current characteristics to compute the shaft power, the results agreed with the results using Eq. (1) to within $\pm 2\%$ (see Fig. 6b). This suggests that other losses, such as damping losses, are much smaller in comparison.

The optimal operating frequencies are 60 Hz, 57.5 Hz and 55 Hz at 28 bar, 24 bar and 20 bar, respectively. This is due to the fact that higher fill pressures lead to a higher effective gas spring stiffness in the compression space. Hence, the overall spring stiffness increases and this leads to higher resonant frequencies.

3. Numerical model validation

Sage [11] is an object-oriented software that allows the user to build a model of a Stirling cryocooler (or engine) by connecting together elemental components of cryocoolers such as heat exchangers, pistons and compression spaces. The model is widely used in the cryocooler industry and is a popular design tool [12–15]. For this study, a numerical Sage model based on the in-line SPTC described above was created. The values for the reference temperatures in the Sage model are set to the values recorded via thermocouples in the experiments. A list of all the inputs to the Sage model along with their typical range is shown in Table 1.

The SPTC was experimentally tested for a range of different fill pressures and sensitivity to frequency and shaft power was examined. In this section, the performance of the SPTC is assessed against the predictions given in Sage, thus allowing for a thorough assessment of the accuracy and reliability of the Sage model.

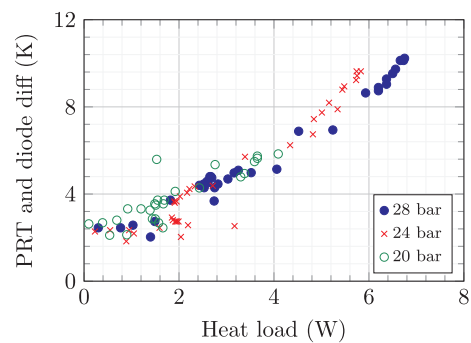


Fig. 4. Difference between the cold end temperature measurements of the PRT and the silicon diode cryogenic temperature sensor against heat load at different fill pressures (PRT used as reference).

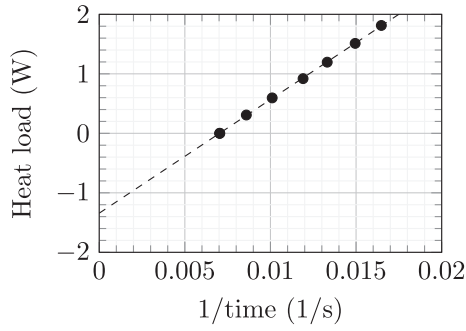


Fig. 5. Static losses of the SPTC when switched off at $T_c = 65$ K. Time logged from $T_c = 75$ K to $T_c = 85$ K. The vertical axis intercept suggests the static losses are 1.3 W.

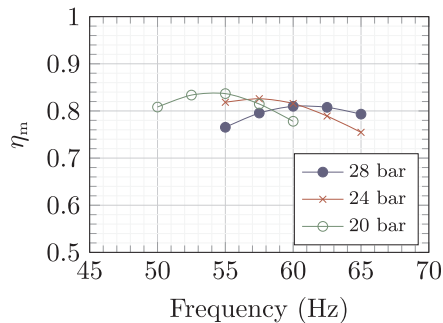
3.1. Sensitivity to frequency

The performance of the SPTC at $T_c = 80$ K was examined at a range of different frequencies and at three different fill pressures. The compressor and displacer strokes were fixed at 9.0 mm and 4.8 mm, respectively. A constant phase angle of 41° was also maintained during this test. The cooling power of the cryocooler, Q_c , is equivalent to the heat load applied by the Lakeshore PID temperature controller in order to maintain a constant T_c . Cooling power as a function of frequency at different fill pressures at $T_c = 80$ K is shown in Fig. 7. The numerical Sage results are also shown alongside the experimental results. Total shaft power, \dot{W}_{sh} , is also shown and is calculated using

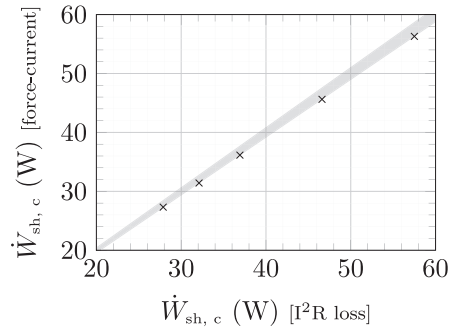
$$\dot{W}_{sh} = \dot{W}_{sh,c} + \dot{W}_{sh,d}, \quad (3)$$

where $\dot{W}_{sh,d}$ is the displacer shaft power. The displacer shaft power was found to be small except for the highest operating frequencies where the displacer motor is running well above its resonant frequency. In order to improve the SPTC overall efficiency, the displacer also needs to operate near resonance. However, it was not possible to adjust the active displacer resonance for this study.

Notably, higher cooling powers are observed at higher fill pressures. This is because higher fill pressures lead to greater peak-to-peak pressure values. This leads to greater gross cooling as the expansion power at the cold end increases. Given that the static losses have not changed significantly, this increase in fill pressure leads to an increase in net cooling values as well. This trend will continue until other losses, such as those related to pressure drop and heat transfer, start to dominate. Furthermore, although increasing the frequency leads to greater cooling power, it also requires greater shaft power. Given that the rise in \dot{W}_{sh} is steeper than Q_c , the overall SPTC efficiency will gradually decrease as the operating frequency increases beyond 65 Hz.



(a) Motor efficiency against frequency for different fill pressures at $T_c = 80$ K.



(b) Shaft power calculations at a fill pressure of 28 bar with $T_c = 80$ K.

Fig. 6. Motor efficiency against operating frequency is shown on the left and the correlation between the two shaft power calculations is shown on the right. The shaded region indicates the $\pm 2\%$ margin.

Table 1
Sage inputs.

| Input | Typical Range |
|-----------------------------------|---------------|
| Fill pressure | 20–31 bar |
| Frequency, f | 50–62.5 Hz |
| Compressor Stroke, d_c | 5–9 mm |
| Displacer Stroke, d_d | 4.8 mm |
| Displacer phase angle, ϕ_d | 10–70° |
| Cold end temperature, T_c | 80, 120 K |
| Heat rejection temperature, T_h | 300–305 K |
| Pulse tube warm end temperature | 295–300 K |
| Compressor body temperature | 295–300 K |
| Water temperature | 293 K |

With regards to the numerical results, the Sage model predicts similar shaft power values to those observed in the experiments, Fig. 7b, but predicts higher cooling power values, Fig. 7a. Although the cooling power values are higher in the Sage model, it does predict the correct trends. Moreover, the experimental and numerical results show similar gains in cooling power with increasing frequency and fill pressure (Fig. 7a). Here are two possible reasons for the discrepancy between the Sage model and the experimental data:

1. The higher cooling power in Sage suggests that the numerical model is underestimating the losses within the SPTC. One of the reasons for this is that the physical SPTC has complicated geometries and volumes, especially in the displacer body where the output from the compressor is connected to the back side of the active displacer and the warm end of the regenerator (Fig. 2). The Sage model does not take into account three dimensional flow effects and assumes simple cylindrical manifolds. Hence, in the experiments there will be a lot more flow mixing than assumed in the Sage model and this may lead to an additional pressure drop and higher losses.
2. There are also uncertainties about the convective losses in the pulse tube assumed in the Sage model. The model assumes the gas within the pulse tube oscillates back and forth with a uniform velocity profile. It then accounts for non-uniform behaviour and wall heat transfer losses by specifying parameters derived from empirical relationships. It is difficult to tune the parameters in Sage to accurately reflect how the gas behaves within the pulse tube and for this study the default Sage values have been used. There are plans to improve our understanding of the flow behaviour using computational fluid dynamics (CFD) techniques. The Sage parameters can then be tuned to better reflect the real SPTC and this should result in better predictions of cooling power.

In order to assess the Sage predictions in more detail, the pressure

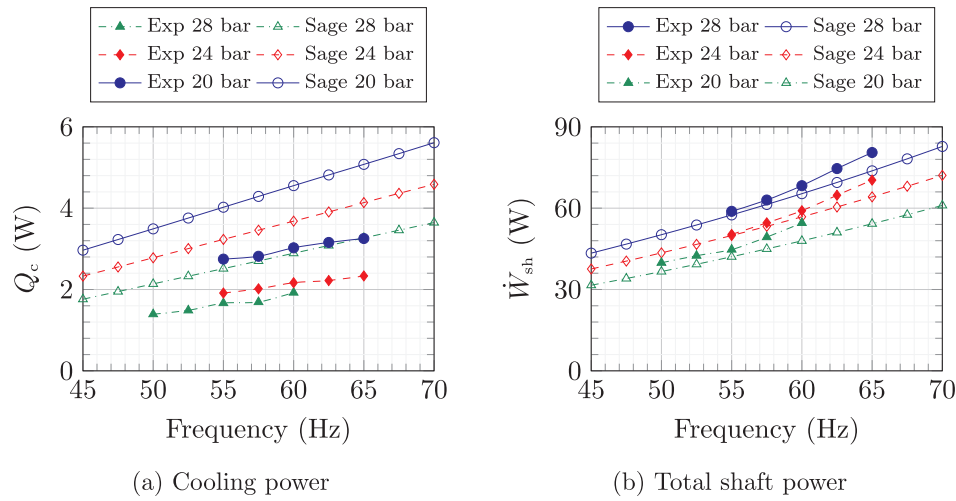


Fig. 7. Cryocooler performance as a function of frequency at different fill pressures with $T_c = 80$ K, $d_c = 9.0$ mm, $d_d = 4.8$ mm and $\phi_d = 41^\circ$.

pulses either side of the cold head assembly predicted by the model are compared against those obtained using pressure transducers in the experiments. Table 2 shows the peak-to-peak values for the pressure pulses (P_1 and P_2) as well as the peak-to-peak pressure drop values across the cold head assembly ($P_1 - P_2$). To reduce the noise in the pressure transducer signals, Fourier analysis was carried out and the profiles were reconstructed using the first three harmonics. Fig. 1 shows the locations where P_1 and P_2 were measured.

The Sage predictions for the peak-to-peak pressure pulses are 17–26% higher than the experimental ones. This is because it underestimates the losses within the system due to the complex geometries mentioned earlier. Despite this, the predicted pressure drops across the cold head assembly are in good agreement with the experimental data and are within 5%. This suggests that the cold head assembly model provides a reasonable representation of what happens in the real system. Hence, the Sage model is able to predict the correct trends, even though it overestimates the cooling power values.

3.2. Sensitivity to shaft power

Fig. 8 shows how cooling power varies with total shaft power when operating at 55 Hz with $T_c = 80$ K and $T_c = 120$ K. Contours of specific power (W/W) are also shown. The variation in shaft power is achieved by varying the linear compressor stroke from 5 mm to 9 mm. A displacer stroke of 4.8 mm and a phase angle of 42° was maintained during this test.

Once again, higher fill pressures led to greater cooling power. This is due to the fact that, as explained previously, higher fill pressures result in greater expansion power at the cold end due to higher peak-to-peak pressures. However, less work is required to displace the pistons at lower fill pressures and the same compressor stroke can be achieved with less shaft power. Given that the results from the different fill pressures appear to fall on one line, this suggests that for this cryocooler

the gains in cooling power at higher fill pressures are proportional to the increase in required shaft power. Hence, the specific power profile appears independent of fill pressure. However, the higher cooling powers can only be achieved at higher fill pressures.

The Sage model was used to mimic these experiments and the numerical results are also shown in Fig. 8. The numerical results for the different fill pressures overlap in the same manner as the experimental results. Moreover, the gradients in the Sage model are similar to the experimental data, especially at $T_c = 120$ K (Fig. 8b). Overall, despite overestimating the cooling power, the Sage model is shown to be capable of predicting the correct trends in the performance of the SPTC.

4. Phase optimisation

4.1. Displacer phase sensitivity

One of the main advantages of having an active displacer is the ability to optimise the cryocooler performance by adjusting the phase between the displacer and the compressor. Initially, sensitivity to phase at a fill pressure of 31 bar was assessed experimentally and the results were reproduced using the Sage model. For this test an operating frequency of 62.5 Hz was used and the compressor and displacer strokes were fixed at 9 mm and 4.8 mm, respectively. Two different cold end temperatures of 80 K and 120 K were considered. The variation in cooling power and relative Carnot efficiency is shown in Fig. 9. The relative Carnot efficiency is calculated using

$$\eta_r = \frac{Q_c}{W_{sh}} \left(\frac{T_h}{T_c} - 1 \right), \quad (4)$$

where T_h is the heat rejection temperature. This is taken as the displacer body temperature (T_3 in Fig. 1) since the warm end of the regenerator and the displacer sit in the same aluminium solid body. This temperature was not fixed and varied from 300 K to 305 K throughout this

Table 2

The peak-to-peak pressure pulse values either side of the cold head assembly (P_1 and P_2) for the tests shown in Fig. 7 operating at 55 Hz. Fig. 1 shows the locations where P_1 and P_2 were measured. The pressure drop across the cold head assembly, $P_1 - P_2$, is also presented.

| Fill pressure (bar) | P_1 | | | P_2 | | | $P_1 - P_2$ | | |
|------------------------|-------------|------|----------|-------------|------|----------|-------------|------|----------|
| | pk-pk (bar) | | | pk-pk (bar) | | | pk-pk (bar) | | |
| | Exp | Sage | Diff (%) | Exp | Sage | Diff (%) | Exp | Sage | Diff (%) |
| 28 | 5.11 | 6.05 | +18.4 | 3.97 | 4.91 | +23.7 | 1.14 | 1.14 | 0.0 |
| 24 | 4.32 | 5.17 | +19.7 | 3.26 | 4.13 | +26.7 | 1.06 | 1.04 | −1.9 |
| 20 | 3.68 | 4.32 | +17.4 | 2.68 | 3.37 | +25.7 | 1.00 | 0.95 | −5.0 |

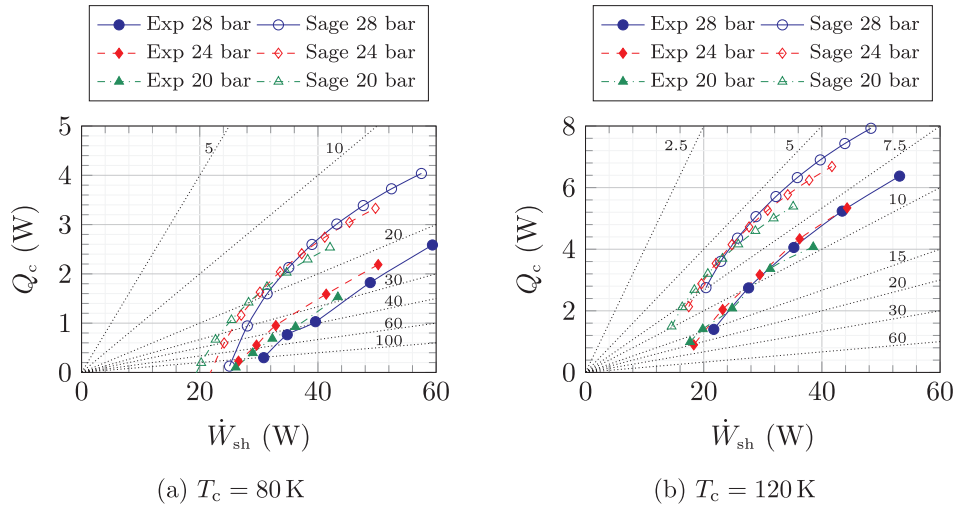


Fig. 8. Cooling power as a function of total shaft power at different fill pressures. The operating frequency was 55 Hz with $d_d = 4.8$ mm and $\phi_d = 42^\circ$. The dotted lines represent contours of specific power (W/W).

study.

The experimental results suggest an optimal phase angle for cooling power and a different one for relative Carnot efficiency. Similarly, the Sage model also predicts two different optimal phase angles and the optimal values are similar to those observed in the experiments. At $T_c = 80$ K maximum cooling power occurs around $\phi_d = 50^\circ$ in both model and experiments and at $T_c = 120$ K the highest cooling power occurs at a higher phase angle of $\phi_d = 55^\circ$ in both model and experiments. Moreover, the experimental data and the Sage predictions both suggest that the maximum relative Carnot efficiency occurs at a phase angle of 40° for both T_c values. Furthermore, broader peaks are observed in the experimental data at $T_c = 120$ K for both cooling power and relative Carnot efficiency and this is also reflected in the Sage model results.

In order to check if fill pressure has any influence on the optimal phase value, the phase sensitivity study was extended to lower fill pressures. Fig. 10 shows the SPTC performance as a function of displacer phase at $T_c = 80$ K. The operating frequencies were 62.5 Hz, 60 Hz and 57.5 Hz at 28 bar, 24 bar and 20 bar, respectively. The results from the numerical Sage model are also shown.

Based on the results, maximum cooling power occurs at around $\phi_d = 50^\circ$ and the highest efficiency is observed at around $\phi_d = 40^\circ$ in both model and experiments. At peak efficiency, the SPTC operating with a fill pressure of 28 bar produces 3.8 W of cooling at $T_c = 80$ K with 69 W of total shaft power ($\dot{W}_{in} = 88$ W). This corresponds to a relative

Carnot efficiency of 15.7% and a specific power of 18 W/W (23 W/W based on \dot{W}_{in}). Noticeably, the optimal values observed in Fig. 10 are very similar to those in Fig. 9. This suggests that fill pressure and small changes to operating frequency do not significantly affect the optimum phase values.

4.2. Relationship between mass flow and pressure pulse

The reason for the variations in cooling power and relative Carnot efficiency observed in Figs. 9 and 10 is because the variation in phase alters the behaviour of the mass flow relative to the pressure pulse at the cold end. Experimental data on mass flow was not available, however the Sage model allows mass flow data to be extracted. The Sage model has predicted the pressure pulse either side of the cold head assembly well (Table 2) and is capable of predicting the correct trends in cooling power and relative Carnot efficiency (Figs. 7–10). Therefore, the mass flow variation in the experiments is expected to follow a similar trend to that predicted by the Sage model. To that effect, the Sage model was used to expand on the behaviour of the mass flow and the pressure pulse within the SPTC.

Fig. 11 shows how the mass flow and the pressure pulse vary in the Sage model at the cold end for three different displacer phase angles at $T_c = 80$ K and a fill pressure of 31 bar. The mass flow at the warm end is also shown. Given that there is very little pressure drop across the pulse tube, the pressure pulse at the warm end is very similar to that at the

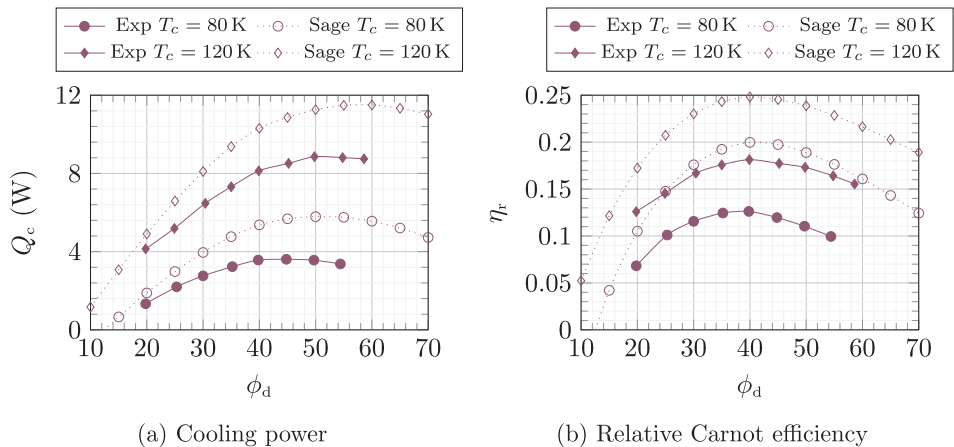


Fig. 9. Cryocooler performance as a function of displacer phase (ϕ_d) at a fill pressure of 31 bar with an operating frequency of 62.5 Hz.

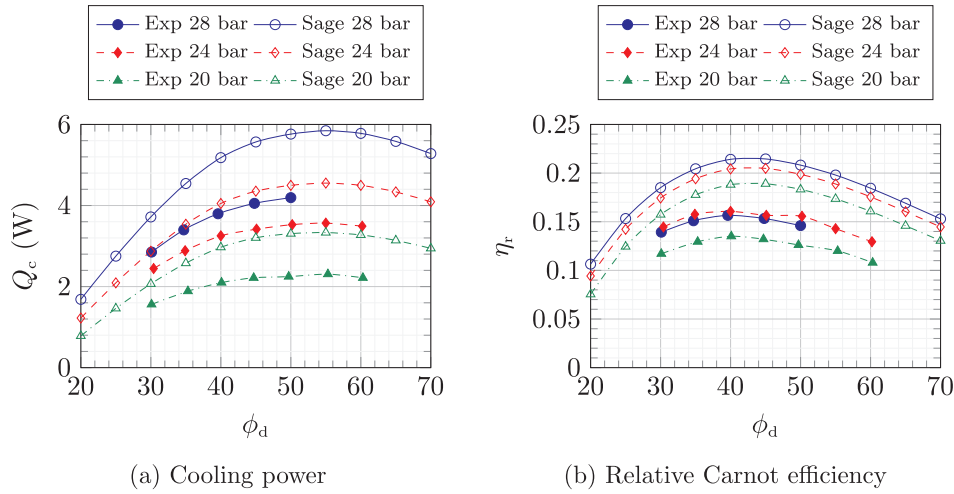


Fig. 10. Cryocooler performance as a function of displacer phase (ϕ_d) at $T_c = 80$ K at three different fill pressures of 28 bar, 24 bar and 20 bar.

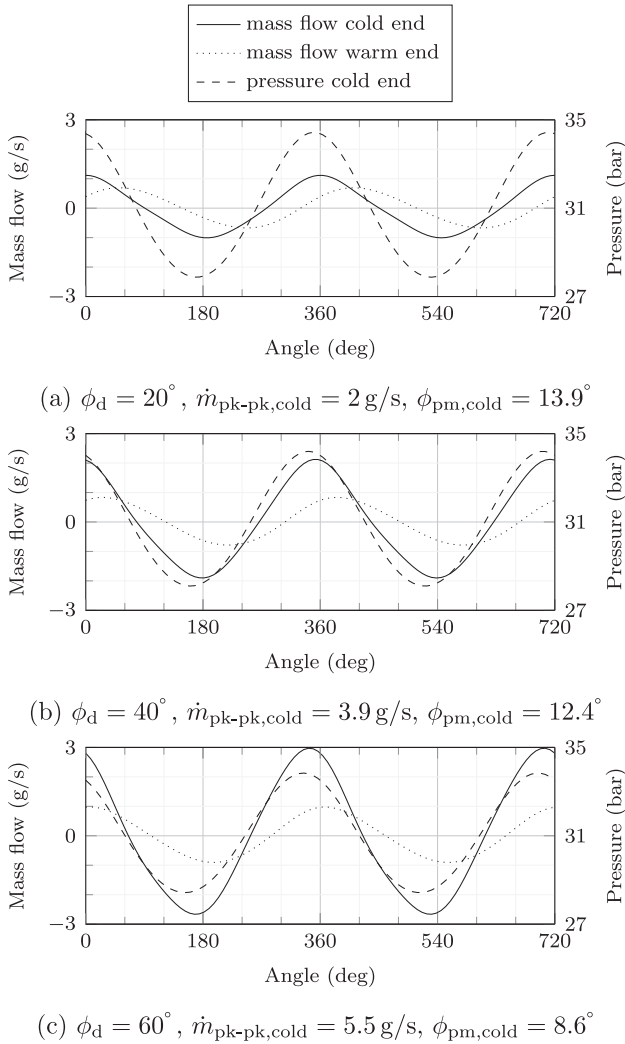


Fig. 11. Mass flow and pressure pulse at the cold end for different values ϕ_d at $T_c = 80$ K from Sage.

cold end and it is therefore not shown.

The phase angle between the pressure pulse and the mass flow, ϕ_{pm} , at the cold end only changes from 13.9° to 8.6° as the displacer phase angle is increased by 40° . However, the peak-to-peak mass flow has

increased from 2 g/s to 5.5 g/s. This increase in mass flow amplitude results in an increase in expansion power at the cold end which leads to an increase in cooling power. Phase angle is also important because a similar cooling power of around 5.5 W is achieved at both $\phi_d = 40^\circ$ and $\phi_d = 60^\circ$ (Fig. 9a) despite the fact that the peak-to-peak mass flow at $\phi_d = 40^\circ$ is 30% smaller at 3.8 g/s. Furthermore, the variation in the pressure pulse at the cold end is less significant and the peak-to-peak value drops from 6.5 bar to 5.4 bar as the displacer phase angle increases from 20° to 60° .

The variation in mass flow peak-to-peak and phase values (relative to pressure pulse) at both the cold end and the warm end are shown in Fig. 12. As mentioned earlier, varying the displacer phase angle has a significant effect on the peak-to-peak mass flow at the cold end, without having a significant effect on the phase between the pressure pulse and the mass flow at the cold end. On the other hand, at the warm end the peak-to-peak values are not significantly affected but the phase angle between the pressure pulse and mass flow drops by more than 40° . This appears unintuitive at first as only a change in phase is expected at the cold end. However, remember that the back space of the displacer is connected to the warm end of the regenerator (Fig. 2) and therefore the slightest variation in displacer phase results in significant changes to the behaviour of the mass flow at the cold end.

Moreover, it was speculated that the 480 mm long copper tube connecting the warm end of the pulse tube to the displacer (see Fig. 2) might be acting as an inductance tube. However, according to Sage, the phase change across the tube is only a few degrees. This suggests that the tube does not act as an inductance tube.

5. Displacer vs inductance tube

In order to demonstrate the advantages of using a displacer, the active displacer in the Sage model was replaced with an inductance tube and a one litre reservoir. Using a smaller reservoir volume will lead to lower efficiency values and a larger volume would not be practical. The Sage optimisation tool was used to find the optimal inductance tube length and diameter. A fill pressure of 28 bar was used with an operating frequency of 60 Hz. The compressor stroke was fixed to 8 mm and the objective function was set to maximise efficiency. The optimised dimensions were found to be an inductance tube with a 2.5 mm internal diameter and a 2.56 m length. The SPTC with a single inductance tube produced 5.26 W of cooling for 115.0 W of shaft power. This corresponds to a relative Carnot efficiency of 12.6%. According to the Sage model, the equivalent active displacer SPTC (with a displacer phase angle of $\phi_d = 40^\circ$) produces 4.90 W of cooling for 62.7 W of shaft power, corresponding to 21.5% relative Carnot efficiency.

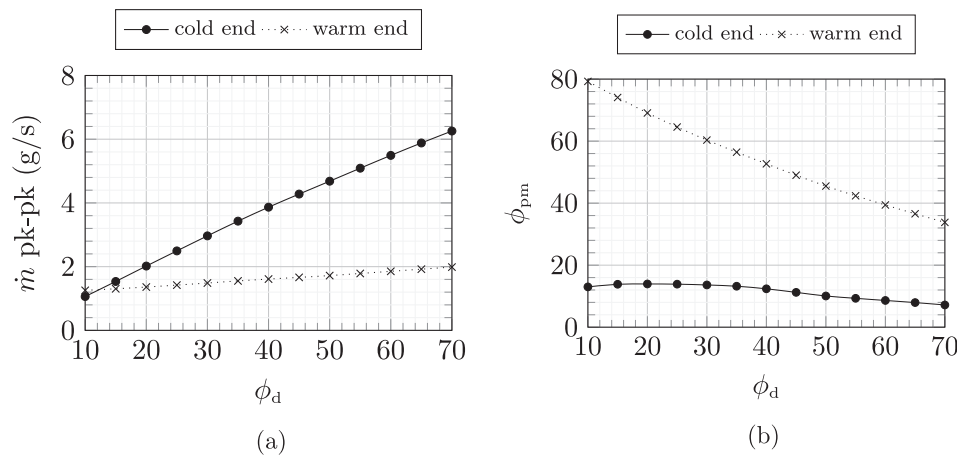


Fig. 12. Mass flow peak-to-peak and phase (relative to pressure pulse) for different displacer phase angles at $T_c = 80$ K from Sage.

Table 3

Sage model: displacer vs inertance tube.

| SPTC type | Shaft Power \dot{W}_{sh} (W) | Cooling Power Q_c (W) | Rel Carnot eff η_r (W) |
|-------------------------|-----------------------------------|----------------------------|--------------------------------|
| Displacer | 62.7 | 4.90 | 0.215 |
| Inertance (single tube) | 115.0 | 5.26 | 0.126 |
| Inertance (two tubes) | 123.6 | 7.80 | 0.174 |

Using two inertance tubes rather than a single one can lead to higher efficiencies and this was also explored using the Sage model. Once again, the Sage optimisation tool was used to find the optimal dimensions for the two inertance tubes. The optimal dimensions were found to be an internal diameter of 2.3 mm and a length of 1.11 m for the first tube (closest to the pulse tube) and an internal diameter of 4.4 mm and a length of 3.07 m for the second tube (closest to the reservoir). The SPTC with two inertance tubes produced 7.80 W of cooling for 123.6 W of shaft power. This corresponds to a relative Carnot efficiency of 17.4%. This is an improvement on the single inertance tube SPTC, but still less efficient than the active displacer SPTC. The results from all three SPTC models are summarised in Table 3.

The inertance tube SPTCs produce more cooling but the shaft power values are significantly higher than the equivalent active displacer SPTC. This is because the volume of gas that needs to be displaced is a lot higher and therefore the inertance tube SPTCs will require more powerful linear compressors. Overall, the SPTC with an active displacer leads to higher relative Carnot efficiency values (Table 3). This is primarily because when using a displacer the expansion work at the warm end of the pulse tube is fed back into the system, whereas when using an inertance tube this expansion power is simply dissipated as heat. Furthermore, the active displacer used in this study can be replaced with a free moving displacer designed to operate at the optimal displacer phase angle. This will result in a much more compact assembly. Hence, another advantage of using a displacer is the possibility of manufacturing more compact SPTCs without the need for long inertance tubes and large reservoirs.

6. Conclusions

An SPTC with an active displacer has been successfully built and tested. The key findings are:

1. Both cooling power and relative Carnot efficiency have optimum phase values. These values differ slightly but they are not critical and there is a range which allows high efficiency and cooling to be simultaneously achieved.

2. Using the Sage model it was shown that varying the displacer phase angle boosts cooling power and relative Carnot efficiency by increasing the magnitude (and not the phase) of the mass flow at the cold end.
3. Using the Sage model the active displacer SPTC was shown to operate more efficiently than an equivalent optimised inertance tube SPTC.

Future plans include investigating the effect of varying the displacer stroke as well as phase and the use of CFD to further refine the flow within the pulse tube in order to improve performance.

Acknowledgement

The authors acknowledge the support of Honeywell Hymatic during the design and manufacture of the SPTC. The authors further acknowledge support from the EPSRC under research project EP/N017013/1.

References

- [1] Radebaugh R. Development of the pulse tube refrigerator as an efficient and reliable cryocooler. *Proc Inst Refrig* 2000;96:11–31.
- [2] Kittel P. Ideal orifice pulse tube refrigerator performance. *Cryogenics* 1992;32(9):843–4.
- [3] Wang C, Wu P, Chen Z. Numerical modelling of an orifice pulse tube refrigerator. *Cryogenics* 1992;32(9):785–90.
- [4] Storch PJ, Radebaugh R. Development and experimental test of an analytical model of the orifice pulse tube refrigerator. *Adv Cryog Eng* 1988;33:851–9.
- [5] Gardner D, Swift G. Use of inertance in orifice pulse tube refrigerators. *Cryogenics* 1997;37(2):117–21.
- [6] De Boer P. Performance of the inertance pulse tube. *Cryogenics* 2002;42(3):209–21.
- [7] Zhu S, Matsubara Y. Numerical method of inertance tube pulse tube refrigerator. *Cryogenics* 2004;44(9):649–60.
- [8] Brito M, Peskett G. Experimental analysis of free warm expander pulse tube. *Cryogenics* 2001;41(10):757–62.
- [9] Zhu S, Nogawa M. Pulse tube stirling machine with warm gas-driven displacer. *Cryogenics* 2010;50(5):320–30.
- [10] Shi Y, Zhu S. Experimental investigation of pulse tube refrigerator with displacer. *Int J Refrig* 2017;76:1–6.
- [11] Gedeon D. Sage: object-oriented software for cryocooler design. *Cryocoolers* 1995;8:281–92.
- [12] Gedeon D. DC gas flows in Stirling and pulse-tube cryocoolers. *Cryocoolers* 1997;9:385–92.
- [13] Wilson K, Gedeon D. Status of pulse tube cryocooler development at Sunpower, Inc. *Cryocoolers* 2005;13:31–40.
- [14] Liu D, Dietrich M, Thummes G, Gan Z. Numerical simulation of a GM-type pulse tube cryocooler system: Part I. Characterization of compressors. *Cryogenics* 2017;81:8–13.
- [15] Liu D, Dietrich M, Thummes G, Gan Z. Numerical simulation of a GM-type pulse tube cryocooler system: Part II. Rotary valve and cold head. *Cryogenics* 2017;81:100–6.